Tracking Optical Welding through Groove Modes in Plasmonic Nanocavities

J. Mertens,[†] A. Demetriadou,[‡,§] R. W. Bowman,[†] F. Benz,[†] M.-E. Kleemann,[†] C. Tserkezis,[‡] Y. Shi,[∥] H. Y. Yang,[∥] O. Hess,[§] J. Aizpurua,[‡] and J. J. Baumberg*[,†]

[†]NanoPhotonics Centre, Cavendish Laboratory, University of Cambridge, Cambridge, CB3 0HE, United Kingdom
[‡]Centro de Física de Materiales, Centro Mixto CSIC-UPV/EHU, and Donostia International Physics Center (DIPC), Paseo Manuel Lardizabal 4, 20018 Donostia-San Sebastian, Spain
[§]Blackett Laboratory, Department of Physics, Imperial College London, London SW7 2AZ, United Kingdom
[∥]Pillar of Engineering Product Development, Singapore University of Technology and Design, Singapore 138682, Singapore

S *Supporting Information*

ABSTRACT: We report the light-induced formation of conductive links across nanometer-wide insulating gaps. These are realized by incorporating spacers of molecules or 2D monolayers inside a gold plasmonic nanoparticle-on-mirror (NPoM) geometry. Laser irradiation of individual NPoMs controllably reshapes and tunes the plasmonic system, in some cases forming conductive bridges between particle and substrate, which shorts the nanometer-wide plasmonic gaps geometrically and electronically. Dark-field spectroscopy monitors the bridge formation in situ, revealing strong plasmonic mode mixing dominated by clear anticrossings. Finite difference time domain simulations confirm this spectral evolution, which gives insights into the metal filament formation. A simple analytic cavity model describes the observed plasmonic mode hybridization between tightly confined plasmonic cavity modes and a radiative antenna mode sustained in the NPoM. Our results show how optics can reveal the properties of electrical transport across well-defined metallic nanogaps to study and develop technologies such as resistive memory devices (memristors).

KEYWORDS: Plasmonic nanocavities, 2D materials, nanoparticle on mirror, tuneable plasmonics, light-induced plasmonic welding, plasmonic hybridisation
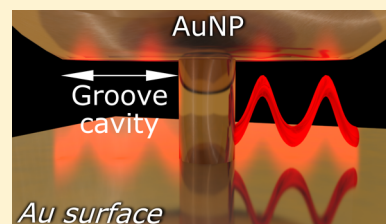
L ight confinement between nanoplasmonic components is now possible in nanoscale gaps and provides exquisitely sensitive spectral information about the realm of subnanometer structures. The unprecedented strong field enhancement in nanoscale gaps allows access to real-time measurements of the movement of atoms and molecules.[1−3] A particularly promising geometry is the nanoparticle-on-mirror (NPoM) composed of a metal nanoparticle placed above a metal mirror, which is a highly versatile system to study fundamental properties of isolated plasmonic junctions.[2,4,5] Its easy and reliable fabrication allows the monitoring of nanoscale reconstructions[1,6] as well as chemical reactions,[7−9] and the exploitation of strong plasmonic enhancements for studying surface enhanced Raman scattering (SERS)[10−12] and photoluminescence (PL).[13,14] Here, we demonstrate the optically induced formation and control of conductive bridges across gaps between the two nanoplasmonic interfaces of the NPoM geometry. Understanding and controlling the growth of such conductive connections is crucial for the development of resistive memory (or "memristive") storage and switching devices. These devices depend on the electrochemical formation and breaking of conductive links used for ultrahigh density information storage, as well as for new generations of high-frequency tunnelling transistors.[15,16] Our results show that conductive bridges

forming due to the migration of metal atoms in a metallic junction can be directly observed optically,[17] through the formation of several laterally-confined gap modes. By modeling these modes, a new route to the understanding and development of nanoscale devices such as memristors is provided.[18,19]

In nanometer-sized plasmonic cavities with gap sizes from $d = 0.6$ to 1.4 nm, we show that laser irradiation can controllably change the cavity morphology at the nanoscale. We use thin spacer materials to separate Au nanoparticles (AuNPs) from a flat Au mirror surface and form an ultranarrow cavity. Such cavities are formed between the facets of AuNPs (Supporting Information Part A), which have typical facet widths $w = 20−30$ nm, and the underlying metal mirror. We then reshape this ultranarrow cavity by irradiation with light, which tunes the plasmonic resonances of the system.[20,21] The ultraviolet (UV) illumination mobilizes the outer Au atoms of the AuNP, which migrate toward the gap, thus increasing the facet size.[7,8,25] While optically manipulating the cavity geometry, dark-field spectroscopy is employed to monitor the
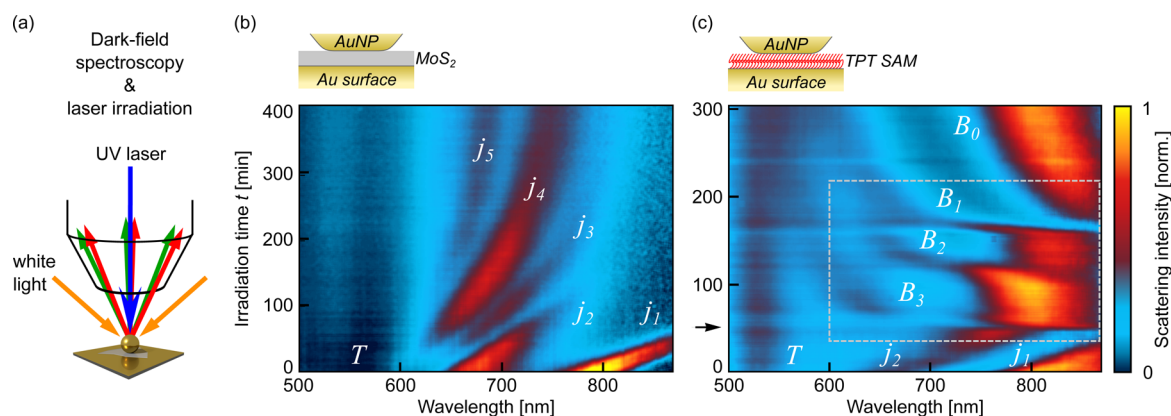
Figure 1. (a) Schematic dark-field spectroscopy of a single NPoM with laser irradiation. (b,c) Color plot of normalized dark-field scattering spectra as a function of irradiation time for individual (b) MoS$_2$ NPoM and (c) TPT NPoM. The dashed box is analyzed in Figure 3; the arrow highlights a discontinuous transition between two regimes discussed below.

plasmonic resonances in situ. We compare different spacer materials, of both inorganic and organic composition, and identify the formation of thin bridges within the NPoM cavity for certain spacer types. Bridge formation is observed in the spectrum through rapid spectral shifts of the plasmonic modes and is accompanied by strong anticrossing features in the spectral signature of the NPoM, highlighting the hierarchy of coupling mechanisms.[22]

In our studies, we use robust monolayers of inorganic molybdenum disulfide (MoS$_2$, 0.6 nm thick) and softer organic self-assembled molecular monolayers (SAMs) of 1,1',4',1''-terphenyl-4-thiol (TPT, 1.4 nm thick) to separate faceted 80 nm AuNPs from a flat Au surface (for fabrication details see Methods). Sparsely drop-cast AuNPs ensure that individual NPoMs can be characterized optically in a customized dark-field microscope. To activate the Au-atom migration, we irradiate individual NPoMs with a 447 nm continuous-wave laser of intensity 0.2 mW power, focused to a diffraction limited spot on the sample. After each irradiation step of 1 s, the laser is turned off, and a dark-field scattering spectrum of the NPoM is recorded (Figure 1a).

The Au NPoM supports several plasmonic resonances visible in its dark-field scattering spectra when irradiating with white light at an angle of incidence of 69° (see Methods for details). One resonance corresponds to a transverse (T-mode) collective electron oscillation at the nanoparticle (NP), oriented parallel to the gold mirror.[23−26] This mode couples only weakly to the surface modes at the underlying Au substrate. Its resonance wavelength is thus close to the resonance of an uncoupled nanoparticle at 530 nm.[27] In contrast, plasmon oscillations in the NP perpendicular to the surface induce image charges within the Au mirror. In this picture, the plasmonic AuNP couples to its image in the gold mirror, thus shifting the coupled resonances into the near-infrared (NIR). Such wavelength shifts are highly sensitive to the atomistic morphology and optical properties of the gap.[1,4,5,26,28,29] The alignment of the lower NP facet against the flat mirror creates an ultrathin plasmonic cavity that supports multiple "cavity" resonances, defined by the geometry (or faceting) of the AuNP.[1,22] These resonances are clearly visible in the initial scattering spectra at time $t = 0$ (Figure 1b,c).

The dark-field scattering spectra of a MoS$_2$ NPoM and a TPT NPoM are presented as a function of irradiation time (in minutes) in the color plots of Figure 1b,c. Despite the fact that

the two systems are initially similar, showing two plasmonic cavity resonances (j_1, j_2), they display fundamentally different behaviors after a few minutes of irradiation with the UV laser. This indicates that the Au-atom migration drastically differs between robust and soft spacers, altering in a different way the radiative properties of the cavity system. Several plasmonic resonances are visible for both systems: the transverse T mode is in both cases excited but not affected by laser irradiation. In contrast, the coupled resonances in the red and NIR are irreversibly shifted upon laser irradiation and fundamentally different in the two systems. Laser irradiation of MoS$_2$ NPoMs (Figure 1b) results in continuous red shifting of all surface coupled resonances (j_1, ..., j_5), while irradiation of TPT NPoMs leads to initial red-shifts of coupled resonances (j_1, j_2) followed by a sharp discontinuity (at black arrow on time axis) and subsequent blue-shifts of the plasmonic modes.

A typical MoS$_2$ NPoM (Figure 2a) shows two initial resonances j_1 and j_2, at 794 and 670 nm which both red-shift linearly at rates of 1.5 nm·min^{-1} and 0.88 nm·min^{-1}, respectively. Their intensity decreases after 50 min of UV laser irradiation, and two new modes j_3 (650 nm) and j_4 (610 nm) emerge. Resonance j_3 disappears with further laser irradiation although mode j_4 persists until the end of the measurement ($t = 400$ min), while after 100 min of irradiation another resonance j_5 becomes visible at 600 nm. The initial evolution of a TPT NPoM (Figure 1c) has a very similar signature compared to MoS$_2$ NPoMs with two coupled resonances (at 792 and 653 nm) shifting under UV irradiation at rates of 2.7 nm·min^{-1} and 2.4 nm·min^{-1}. However, after 50 min of irradiation, the sharp discontinuity changes this red-shifting behavior to blue-shifting of multiple modes.

We thus first discuss the origin of the red-shifting behavior, before then concentrating on the new behavior observed with soft spacers, which we show to arise from conducting bridges. We find consistent behavior for all NPoM systems with the same spacer, with minor variations in the red-shift rates and spectral positions (see below). These observations highlight the importance of the permeability (robustness) of the spacer. We also note that to account for what is going on requires electromagnetic modeling since electron microscopy of any sort damages the construct radically, changing all of the spectral resonances and thus cannot be used.[1]

Inorganic "Hard" Spacers. We first consider the observed light-induced red-shifts of plasmonic resonances using a mixed
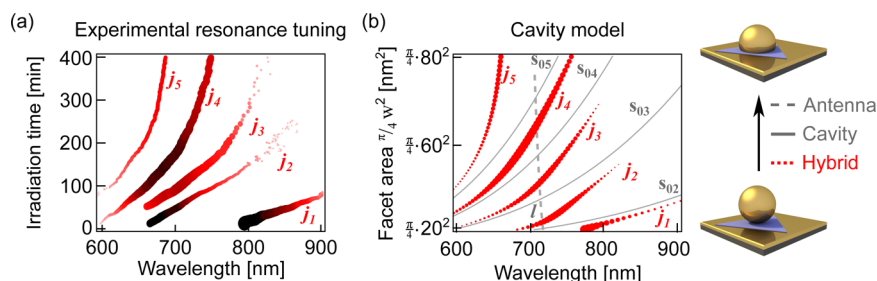
Figure 2. (a) Experimental resonant wavelengths of a MoS₂ NPoM vs UV irradiation time. Marker size and color (black = high intensity, pink = low intensity) both represent the scattered mode intensity. (b) Calculated mode position for a MoS₂ NPoM as a function of facet area $(\pi/4)w^2$ (schematic on the right). Gray-dashed: longitudinal antenna mode l; gray-solid: transverse cavity modes S_{0i}; red-dots: hybrid modes j_i, dot size depicts antenna-mode contribution to the hybrid mode.

cavity-antenna model.[1,22] In comparison to a single spherical scatterer, two tightly coupled plasmonic components support both cavity modes confined to the gap between them (transverse to the axis of symmetry of the NPoM) as well as antennae modes that radiate efficiently (longitudinal to the axis of symmetry of the NPoM). These modes are mixed and radiate at specific angles depending on the exact geometry. For the NPoM system, each faceted nanoparticle couples to its image in the underlying metal mirror, forming subnanometer plasmonic cavities.[1,22] The dispersion of cavity modes s_{0i} as a function of facet length w is calculated based on the metal−insulator−metal (MIM) waveguide dispersion[30,31] with Au cladding and insulator given by a monolayer of MoS₂ with thickness d = 0.6 nm and background dielectric permittivity ε_d = 1.63.[32] In the small gap and within a Drude approximation to describe the metal, the resonance positions λ_i of the cavity modes can be analytically calculated[1] (Figure 2b, solid gray lines) using

$$\lambda_i = \lambda_p \sqrt{\frac{w\varepsilon_d}{d\alpha_i} + \varepsilon_\infty} \tag{1}$$

Here, λ_p = 137 nm is the plasmon wavelength of Au in the Drude approximation with ε_∞ = 10.5 the corresponding background permittivity, and $\alpha_i = \alpha_i' - \psi$ with α_i' = 3.8, 7.0, 10.2, ... being the argument of the ith antinode of the cylindrical Bessel function J_0 accounting for a simplified circular facet shape, while $\psi = \pi$ is a phase-shift that accounts for the reflection of the cavity modes at the cavity edges.[1] Such cavity resonances are strongly confined to the gap region but can radiate into the far-field by coupling to the main plasmonic longitudinal antenna mode l (Figure 2b, dashed gray line).[1,22] The antenna mode is strongly radiative and originates from coupling of plasmonic charge oscillations across the AuNP with induced image charge oscillations in the Au surface (slightly blue-shifting as the NP is reshaped). New strongly coupled hybrid modes j_i are formed, shown as red markers in Figure 2b. An eigenmode analysis of these hybrid modes reveals their radiative strength as a function of wavelength and cavity length, given by the antenna mode fraction of each hybrid mode. While hybrid modes close to the antenna mode radiate efficiently (larger marker size), those modes spectrally far from the antenna mode have a cavity-like character and radiate very weakly into the far-field.

The observed laser-induced spectral red-shifts can then be explained by a steadily increasing size of the NP facet (Supporting Information Part F). Comparison of the simple cavity model (Figure 2b) with the experimental red-shifting results (Figure 2a) shows excellent agreement. Particles with

very small facet sizes w < 10 nm are not observed experimentally for 80 nm AuNPs (since nanoparticles are never perfectly smooth, Supporting Information Part A). As previously reported,[1] atoms at the AuNP surface are mobilized by laser irradiation and migrate to the gap region, thus increasing the facet size. Our results here suggest that the facet area increases linearly with time (so UV irradiation delivers a constant Au atom flux to the lower facet). While this may result from local heating via optical absorption, irradiating with red light where the AuNPoM has a larger absorption cross section still results in similar red-shift rates. This suggests that light can reduce barriers to surface site hopping, reduce the Au−Au bond strength, or provide optical forces (these cannot yet be distinguished). The spectral signature is thus exquisitely sensitive to minute changes of the junction morphology, which cannot yet be directly observed using electron microscopy. A deformation of particles is visible with an electron microscope only if NPoMs are irradiated for longer times at higher powers (Supporting Information Part B). We emphasize that UV irradiation does not modify the MoS₂ spacer layer (laser ablation only starts for >10 times larger power[33]). Indeed no changes in the photoluminescence and Raman scattering of MoS₂ are observed before and after the laser irradiation here (Supporting Information Part C).

"Soft" Organic Molecular Spacers. Similar red-shifts from light-induced Au atom migration are first seen when UV illuminating NPoMs with softer molecular spacers, but a sudden discontinuity arises after a variable time. Two regimes can be distinguished: A nonconductive and a conductive regime. In the nonconductive regime, modes shift to the red which is explained as above by facet growth of the particle without perturbing the cavity (Figure 3b,c lower panel). FDTD simulations using an 80 nm NP forming the NPoM cavity with a fixed circular facet size that increases from w = 40 nm to w = 50 nm, provide a good understanding of spectra in the preconductive regime. A sharp transition in the experimental data at an irradiation time of t = 50 min suggests fast morphological changes while the system transitions to the conductive regime. This fast growth regime is indicated in the simulations (Figure 3b) by a gray shaded area, in which the cavity is electronically shorted. Further simulation results (Supporting Information Part N) show within this gray shaded region how Au protrusions from the NP produce fast spectral shifts leading to the groove cavity formation. The distinct threshold for the transition into the conductive regime at a facet size of w = 50 nm is connected to the amount of energy deposited in the cavity (Supporting Information Part G).
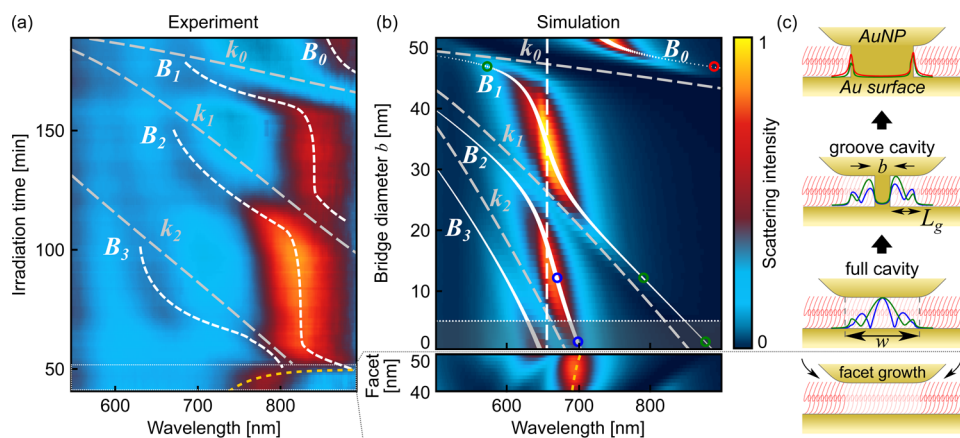
Figure 3. Irradiation of a TPT NPoM with two regimes: Bottom panel mimics the nonconductive and top panel the conductive regime. (a) Detailed experimental dark-field scattering spectra of a TPT NPoM showing tuning of coupled resonances as a function of laser irradiation. Lines are a guide to the eye, highlighting cavity modes. (b) Finite-difference time domain simulations (normalized color map; yellow: high intensity, blue: low intensity) of a TPT NPoM with $w = 51$ nm facet width and central conductive bridge linking NP and surface, of diameter b increased from 0 to 51 nm as indicated in schematic (c). Lines are analytic mode positions of cavity modes (k_i, dashed gray), fixed antenna mode position (dashed white), and calculated hybrid mode positions (white markers, marker size gives antenna mode fraction in the hybrid modes). Gray shaded area from $b = 0$ nm to 5 nm (dotted white line) indicates a fast transition regime from nonconductive to conductive, not captured in the experiment dynamics. (c) Schematic of cavity model with centered cylindrical bridge. Curves show each mode intensity distribution in midgap for corresponding spectral positions of open circles in panel b.

Typically when illuminating a TPT NPoM with this power density, four distinct resonances (B_{0-3}) are observed after the discontinuity (black arrow in Figure 1c, Supporting Information Part N). These resonances blue-shift and eventually merge with the spectral position of the T-mode at 530 nm for prolonged laser irradiation. Initially resonance B_2 barely shifts its spectral position under continued irradiation from $t = 50$ min to $t = 100$ min, before it then anticrosses with B_1 which blue-shifts into the detection range from the NIR. After 160 min of laser irradiation, a similar sharp anticrossing behavior is again observed for mode B_1, this time interacting with the lowest order mode B_0. We now demonstrate that these spectra can be explained by metallic bridging across the insulating TPT spacers, facilitated by the absence of lateral covalent bonding in this molecular spacer layer.

More detailed spectra of this multiple resonance shifting behavior (Figure 3a) show distinct blue-shifting of coupled plasmonic resonances that can be accounted for in finite difference time domain (FDTD) simulations by introducing a growing Au conducting bridge between surface and nanoparticle (Figure 3c). This conductive link has two effects: it leads to a charge transfer between nanoparticle and mirror, and it strongly perturbs the cavity modes. With increasing irradiation time, it appears that such conductive bridges increase in width. As the gap capacitance increases during the initial protrusion that initiates a bridge, the coupled modes are predicted to first red shift, as observed in experiment. Such a process resembles dc field-induced breakdown in dielectric capacitors in which fluctuations can suddenly destabilize the interface.[34] To parametrize the influence of conductive bridges on the spectral far-field response of the NPoM system, FDTD simulations are performed for a TPT NPoM (see Methods for details). For these, an 80 nm AuNP with a fixed circular facet size of diameter $w = 51$ nm is assumed to be progressively conductively connected to the Au surface through a Au bridge in the center of the NP facet (top panel in Figure 3c). The diameter of the cylindrical conductive bridge is varied from $b = 0$ to 51 nm, i.e. from no connection to a bridge with a size that equals the full facet (so metal fully fills the cavity formed by NP facet and Au surface, see schematics in Figure 3c). The color map (Figure 3b) shows the spectral response of the connected NPoM as a function of bridge diameter b. With increasing bridge width, plasmonic resonances shift to the blue, and mode mixing results in an anticrossing behavior. This behavior (Figure 3b) matches our experimental results (Figure 3a) very well, although the vertical irradiation time-axis in the experiment cannot be directly linked to the diameter of the bridge in the simulations due to a nonlinear relationship between them. In addition, exact mode positions in the simulation are influenced by the size of the particle facet (Supporting Information Part I). Although the facet size is kept constant in the simulations, it is possible that laser irradiation simultaneously alters both the conductive bridge size as well as the facet size. However, FDTD simulations evidence that the facet growth slows down considerably after bridges are formed (Supporting Information Part K).

The anticrossing behavior observed in the simulation and experiment can be understood by adapting the previous cavity model that assumed an unperturbed NPoM cavity (bottom schematic of Figure 3c). We compare the simulation data with a simple analytical cavity model, assuming a perturbed cavity length L_g that is defined by the facet diameter w and the bridge diameter b (center schematic of Figure 3c), $L_g = 0.5(w - b)$. Resonant transverse modes of the perturbed cavity (Figure 3c), which are referred to as groove modes[35,36] in the following, are obtained for the resonance condition $L_g = m\lambda_m/2$ and thus have a wavelength of

$$\lambda_m = \frac{w - b}{m + (\varphi/2\pi)} \qquad (2)$$

where $m = 0, 1, 2, \ldots$ is the groove cavity mode order and φ a phase factor to account for the reflection at the particular boundary conditions of the cavity system. This phase factor is necessary for the perturbed cavity because the cavity is terminated on one end by the Au bridge whereas the other termination is set by the edge of the facet (Figure 3c), pushing

the mode toward the facet edges. The energy of these cavity modes is estimated by calculating the groove wavevector $k_m = 2\pi/\lambda_m$ and finding the corresponding energy from the metal−insulator−metal planar waveguide dispersion built of a Au-clad TPT core (Supporting Information Part D). The dispersion relation of the first three cavity groove modes k_m with fixed phase factor $\varphi = 0.4\pi$ (fitted to the simulation results) are plotted as a function of bridge diameter b (gray dashed lines in Figure 3b). These modes indeed shift to the blue with increasing bridge diameter because the cavity length $w - b$ reduces for larger bridge b.

As previously discussed, the cavity MIM modes are strongly confined to the gap region, and although they do not radiate into the far-field, they mix with the longitudinal antenna mode that radiates. We fix the antenna mode at a spectral position of 680 nm (vertical dashed line in Figure 3b) since this is barely perturbed by the bridging, giving spectral positions of hybrid modes calculated by solving for the eigenvalues of the coupled system (Supporting Information Part D). Hybrid groove modes in Figure 3b are white lines whose width corresponds to the strength of the antenna mode (their radiative component). This simple cavity model (white lines) fits the full-wave simulations (color map) extremely well, thus giving a good understanding of the experimental observations as well as the simulations. Extracting the near-field distribution of resonant modes in the bridged NPoM from FDTD shows that these modes evanescently decay inside the bridge, being expelled into the grooves (Figure 3c, Supporting Information Part H). This justifies our use of a shortened cavity, which arises from the perturbation in the gap induced by the bridge. It is however intriguing that the 3D problem of a bridged NPoM can be reduced to a simplified 1D cavity (Figure 3c). Our simulations (Figure 3b) show that first formation of a 1 nm diameter bridge only slightly blue-shifts the unperturbed cavity modes. To relate this to previous theoretical work,[37] we note that if such a bridge possesses bulk Au conductivity the link already has a conductance of $>100G_0$. We recently showed that, in this situation, the conductance is not dominating the response, but the mode position is instead controlled by the kinetic inductance of the conducting wire, giving blue shifts proportional to its diameter as observed in the simulations here.[38] A more careful comparison of the experiment with these simulations suggests that the bridge first appears with a 5 nm diameter (horizontal dotted white line Figure 3b) within the measurement time scale. Observing dark-field scattering spectra while optically irradiating plasmonic constructs thus allows clear identification of the contact morphology and its dynamics, which provides crucial information to develop a theoretical understanding of what drives such nanoscale materials processes. Subsequently any desired conductive bridge width can be selected remaining stable when the UV laser is turned off (for times in excess of many hours), and this is how dark-field spectra are recorded (see Methods Section for details).

So far in our discussion, we assumed that the bridge forms at the exact center of a cavity. However, experimentally it is not obvious at which lateral position a bridge should form under each facet. In the specific experimental results we concentrate on above, a central location fits the simulations well. In fact FDTD simulations growing the bridge at the facet edge show a similar spectral shifting behavior (Supporting Information J). Again, strong mode mixing with several anticrossings of cavity and antenna modes are observed when the bridge diameter is increased. In contrast to the symmetric case with a bridge in the center, the tuning evolution becomes distorted. Such variability in mode tuning is observed experimentally when irradiating many different NPoM with these SAM spacers (Supporting Information L). The results of the effective central location are thus a good representation of the bridging effect in the case of Figure 3.

There are several other parameters that influence the bridge formation, such as the exact nanomorphology and the composition of the spacer material. The robustness of the spacer material explains the differences between MoS_2 and TPT spacers. While MoS_2 monolayers are very robust and continuous, TPT SAMs can be affected more easily and can develop pinholes when irradiated with a laser. Only when the laser power is increased drastically, blue-shifts are found for MoS_2 NPoMs similar to the ones observed for TPT NPoMs (Supporting Information Part B). Furthermore, if a conductive spacer such as a SAM of biphenyl-4-4′-dithiol (BPDT) molecules is employed to realize the NPoM, laser irradiation only marginally affects the coupled resonance position. No blue-shifts of resonances are found, and no spectral signatures that can be linked to the formation of bridges are present (Supporting Information Part M). This behavior is explained by reduced forces in the gap since the cavity between nanoparticle and Au surface is now electronically shorted by these conducting linker molecules.[2]

In conclusion, we present light-induced formation and real-time monitoring of nanoscale Au bridges between individual nanoparticles and a gold surface. Faceted AuNPs on top of Au mirrors form nanometer-high plasmonic cavities that can be manipulated controllably using laser irradiation. These cavities host resonances that can be effectively accounted for analytically using the MIM waveguide dispersion. Laser irradiation of individual NPoMs mobilizes nanoparticle surface atoms which migrate toward the embedded spacer, thus increasing the particle facet size. Such morphological alterations tune a set of cavity resonances, which shift to the red. Pinholes induced in the spacer layer of specific materials result in the formation of thin conductive bridges that electronically and geometrically connect the AuNP with the Au substrate. The main effect of such bridge formation is a geometrical change in the groove cavity length. Continued laser irradiation increases the bridge width, which in turn decreases the cavity length. Resonances in the cavity are expelled from the bridge region and shift to the blue as a function of laser irradiation and bridge width. This behavior is observed experimentally and confirmed by FDTD simulations of the connected NPoM. A simple analytical cavity model describes well the strong coupling between longitudinal antenna mode and transverse cavity modes and predicts plasmonic mode positions in the NPoM structure. Our results show that formation of nanometer sized wires in memristor-like geometries can be directly observed and monitored optically, and their size can be optically controlled with high accuracy. This work allows a much better understanding of how atoms can be tracked and moved by light, opening up opportunities in sensing, quantum metrology, ultralow power devices, and optoelectronics.

Methods. *Sample Fabrication.* The Au substrates are fabricated by template stripping: a layer of 100 nm Au is evaporated on polished silicon wafers. Small silicon substrates (10×10 mm^2) are then glued to the Au surface using epoxy glue (EPOTEK377). The samples are left on a hot-plate for 2 h at a temperature of 150 °C to cure the epoxy glue. After cooling, the top silicon substrates are gently pushed-off, and Au

substrates are thereby stripped off, with Au adhering to the glue and the small Si substrates. The obtained Au surface typically has a roughness of ~0.3 nm.[39]

Gold substrates are covered with molybdenum disulfide (MoS_2) or a self-assembled monolayer of 1,1′,4′,1″-terphenyl-4-thiol (TPT) molecules. Monolayers of MoS_2 are grown by chemical vapor deposition (CVD) on sapphire substrates and transferred to the Au substrates employing a standard transfer method using poly(methyl methacrylate) (PMMA).[40−43] Molecular layers of TPT are self-assembled on Au surfaces by immersing substrates in a 1 mM TPT in anhydrous ethanol solution for 12 h. The samples are then rinsed with ethanol to remove unbound excess thiols and subsequently dried with nitrogen.

Citrate stabilized, 80 nm AuNPs are purchased from BBI Scientific and drop-cast for 60 s on the MoS_2 covered substrates and for 10 s on the TPT coated substrates. The samples are rinsed thoroughly subsequently with deionized water to remove unbound AuNPs.

Dark-Field Spectroscopy and Laser Illumination. Individual NPoMs are characterized optically in a customized microscope (Olympus BX51) using dark-field white-light spectroscopy in reflection geometry. Light is focused with a 100× dark-field microscope objective providing high angle illumination of up to 69° (NA = 0.93) and collection of scattered light with a numerical aperture of NA = 0.8 (Figure 1a). Light collection is performed in confocal geometry using a 50 μm fiber as pinhole to limit the collection area on the sample (1 μm diameter). Spectra are recorded with a cooled spectrometer (Ocean Optics QE65000) and an integration time of 1 s.

Illumination of individual NPoMs is performed using a diode laser (Coherent CUBE) with 447 nm emission wavelength, coupled to the microscope with a single-mode fiber. Collimated laser light fills the back-focal plane of the microscope objective, thus illuminating in bright-field geometry a diffraction limited area of 360 nm diameter on the sample. Particles are irradiated with a power of 0.2 mW (power measured after the objective at the sample position), resulting in a power density of ~0.8 mWμm^{-2}. Samples are placed on a motorized translation stage, and each measurement step is performed as follows: first, the drift is compensated by automated repositioning of the NPoM in the plane and along the focus axis. A chromatic aberration corrected dark-field spectrum is recorded (see de Nijs et al.[32] for details on aberration correction), and the particle is subsequently irradiated with UV for 1s. After irradiation, the laser is turned off, and the process is repeated.

Simulations. The electromagnetic response of the NPoM geometry is simulated by three-dimensional finite-difference time-domain (FDTD) calculations using Lumerical FDTD Solutions v8.12.527. The AuNP is modeled as two ellipsoids merged together, resulting in an overall height of 60 nm and lateral diameter of 80 nm. The height, lateral diameter, and volume are kept constant as the morphology of the nanoparticle changes (Supporting Information Part E). The optical properties of both the nanoparticle and mirror are fitted to Johnson and Christy experimental data for gold.[44] The TPT-spacer is modeled with thickness of 1.1 nm and refractive index of n = 1.45, while the MoS_2-spacer has a thickness of 0.6 nm and refractive index n = 1.27. The system is illuminated with a plane wave polarized perpendicular to and propagating along the mirror. To ensure that fields within the nanocavity are resolved well, extremely fine meshing parameters of 0.3 nm for the TPT and 0.2 nm for MoS_2 spacer are used.

ASSOCIATED CONTENT

Ⓢ Supporting Information

The Supporting Information is available free of charge on the ACS Publications website at DOI: 10.1021/acs.nanolett.6b02164.

    Data sets of irradiated Au NPoMs as well as detailed information on the analytical model and the FDTD simulations (PDF)

AUTHOR INFORMATION

Corresponding Author

*E-mail: jjb12@cam.ac.uk.

Notes

The authors declare no competing financial interest. Data supporting this paper are available at http://dx.doi.org/10.17863/CAM.1302.

REFERENCES

(1) Sigle, D. O.; Mertens, J.; Herrmann, L. O.; Bowman, R. W.; Ithurria, S.; Dubertret, B.; Shi, Y.; Yang, H. Y.; Tserkezis, C.; Aizpurua, J.; Baumberg, J. J. *ACS Nano* **2015**, *9* (1), 825−830.

(2) Benz, F.; Tserkezis, C.; Herrmann, L. O.; de Nijs, B.; Sanders, A.; Sigle, D. O.; Pukenas, L.; Evans, S. D.; Aizpurua, J.; Baumberg, J. J. *Nano Lett.* **2015**, *15* (1), 669−674.

(3) Emboras, A.; Niegemann, J.; Ma, P.; Haffner, C.; Pedersen, A.; Luisier, M.; Hafner, C.; Schimmel, T.; Leuthold, J. *Nano Lett.* **2016**, *16* (1), 709−714.

(4) Ciraci, C.; Hill, R. T.; Mock, J. J.; Urzhumov, Y.; Fernandez-Dominguez, A. I.; Maier, S. a.; Pendry, J. B.; Chilkoti, A.; Smith, D. R. *Science (Washington, DC, U. S.)* **2012**, *337* (6098), 1072−1074.

(5) Mock, J. J.; Hill, R. T.; Degiron, A.; Zauscher, S.; Chilkoti, A.; Smith, D. R. *Nano Lett.* **2008**, *8* (8), 2245−2252.

(6) Grady, N. K.; Knight, M. W.; Bardhan, R.; Halas, N. J. *Nano Lett.* **2010**, *10* (4), 1522−1528.

(7) Ding, T.; Mertens, J.; Sigle, D. O.; Baumberg, J. J. *Adv. Mater.* **2015**, *27* (41), 6457−6461.

(8) Ding, T.; Sigle, D.; Zhang, L.; Mertens, J.; de Nijs, B.; Baumberg, J. *ACS Nano* **2015**, *9* (6), 6110−6118.

(9) Lumdee, C.; Toroghi, S.; Kik, P. G. *ACS Nano* **2012**, *6* (7), 6301−6307.

(10) Sigle, D. O.; Hugall, J. T.; Ithurria, S.; Dubertret, B.; Baumberg, J. J. *Phys. Rev. Lett.* **2014**, *113* (8), 087402.

(11) Mubeen, S.; Zhang, S.; Kim, N.; Lee, S.; Krämer, S.; Xu, H.; Moskovits, M. *Nano Lett.* **2012**, *12* (4), 2088−2094.

(12) Chen, S. Y.; Mock, J. J.; Hill, R. T.; Chilkoti, A.; Smith, D. R.; Lazarides, A. A. *ACS Nano* **2010**, *4* (11), 6535−6546.

(13) Lumdee, C.; Yun, B.; Kik, P. G. *ACS Photonics* **2014**, *1* (11), 1224−1230.

(14) Kern, J.; Trügler, A.; Niehues, I.; Ewering, J.; Schmidt, R.; Schneider, R.; Najmaei, S.; George, A.; Zhang, J.; Lou, J.; Hohenester, U.; Michaelis de Vasconcellos, S.; Bratschitsch, R. *ACS Photonics* **2015**, *2* (9), 1260−1265.

(15) Emboras, A.; Goykhman, I.; Desiatov, B.; Mazurski, N.; Stern, L.; Shappir, J.; Levy, U. *Nano Lett.* **2013**, *13* (12), 6151−6155.

(16) Hoessbacher, C.; Fedoryshyn, Y.; Emboras, A.; Melikyan, A.; Kohl, M.; Hillerkuss, D.; Hafner, C.; Leuthold, J. *Optica* **2014**, *1* (4), 198.

(17) Marchesin, F.; Koval, P.; Barbry, M.; Aizpurua, J.; Sánchez-Portal, D. *ACS Photonics* **2016**, *3* (2), 269−277.

(18) Di Martino, G.; Tappertzhofen, S.; Hofmann, S.; Baumberg, J. *Small* **2016**, *12* (10), 1334−1341.

(19) Celano, U.; Goux, L.; Degraeve, R.; Fantini, A.; Richard, O.; Bender, H.; Jurczak, M.; Vandervorst, W. *Nano Lett.* **2015**, *15* (12), 7970−7975.

(20) Lassiter, J. B.; McGuire, F.; Mock, J. J.; Ciracì, C.; Hill, R. T.; Wiley, B. J.; Chilkoti, A.; Smith, D. R. *Nano Lett.* **2013**, *13* (12), 5866−5872.

(21) Kuhlicke, A.; Schietinger, S.; Matyssek, C.; Busch, K.; Benson, O. *Nano Lett.* **2013**, *13* (5), 2041−2046.

(22) Tserkezis, C.; Esteban, R.; Sigle, D. O.; Mertens, J.; Herrmann, L. O.; Baumberg, J. J.; Aizpurua, J. *Phys. Rev. A: At., Mol., Opt. Phys.* **2015**, *92* (5), 053811.

(23) Hu, M.; Ghoshal, A.; Marquez, M.; Kik, P. G. *J. Phys. Chem. C* **2010**, *114* (16), 7509−7514.

(24) Halas, N. J.; Lal, S.; Chang, W. S.; Link, S.; Nordlander, P. *Chem. Rev.* **2011**, *111* (6), 3913−3961.

(25) Yamamoto, N.; Ohtani, S.; Garcia de Abajo, F. J. *Nano Lett.* **2011**, *11* (1), 91−95.

(26) Nordlander, P.; Prodan, E. *Nano Lett.* **2004**, *4* (11), 2209−2213.

(27) Olson, J.; Dominguez-Medina, S.; Hoggard, A.; Wang, L.-Y.; Chang, W.-S.; Link, S. *Chem. Soc. Rev.* **2015**, *44* (1), 40−57.

(28) Hill, R. T.; Mock, J. J.; Urzhumov, Y.; Sebba, D. S.; Oldenburg, S. J.; Chen, S. Y.; Lazarides, A. A.; Chilkoti, A.; Smith, D. R. *Nano Lett.* **2010**, *10* (10), 4150−4154.

(29) Esteban, R.; Aguirregabiria, G.; Borisov, A. G.; Wang, Y. M.; Nordlander, P.; Bryant, G. W.; Aizpurua, J. *ACS Photonics* **2015**, *2* (2), 295−305.

(30) Kuttge, M.; Cai, W.; García de Abajo, F. J.; Polman, A. *Phys. Rev. B: Condens. Matter Mater. Phys.* **2009**, *80* (3), 033409.

(31) Bozhevolnyi, S. I.; Jung, J. *Opt. Express* **2008**, *16* (4), 2676−2684.

(32) de Nijs, B.; Bowman, R. W.; Herrmann, L. O.; Benz, F.; Barrow, S. J.; Mertens, J.; Sigle, D. O.; Chikkaraddy, R.; Eiden, A.; Ferrari, A.; Scherman, O. A.; Baumberg, J. J. *Faraday Discuss.* **2015**, *178*, 185−193.

(33) Castellanos-Gomez, a.; Barkelid, M.; Goossens, a. M.; Calado, V. E.; Van Der Zant, H. S. J.; Steele, G. a. *Nano Lett.* **2012**, *12* (6), 3187−3192.

(34) Goldberg-Oppenheimer, P.; Steiner, U. *Small* **2010**, *6* (11), 1248−1254.

(35) Gramotnev, D. K.; Bozhevolnyi, S. I. *Nat. Photonics* **2010**, *4* (2), 83−91.

(36) Bermúdez-Ureña, E.; Gonzalez-Ballestero, C.; Geiselmann, M.; Marty, R.; Radko, I. P.; Holmgaard, T.; Alaverdyan, Y.; Moreno, E.; García-Vidal, F. J.; Bozhevolnyi, S. I.; Quidant, R. *Nat. Commun.* **2015**, *6*, 7883.

(37) Perez-Gonzalez, O.; Zabala, N.; Borisov, A. G.; Halas, N. J.; Nordlander, P.; Aizpurua, J. *Nano Lett.* **2010**, *10* (8), 3090−3095.

(38) Benz, F.; de Nijs, B.; Tserkezis, C.; Chikkaraddy, R.; Sigle, D. O.; Pukenas, L.; Evans, S. D.; Aizpurua, J.; Baumberg, J. J. *Opt. Express* **2015**, *23* (26), 33255.

(39) Benz, F.; Chikkaraddy, R.; Salmon, A.; Ohadi, H.; de Nijs, B.; Mertens, J.; Carnegie, C.; Bowman, R. W.; Baumberg, J. J. *J. Phys. Chem. Lett.* **2016**, *7* (12), 2264−2269.

(40) Zhan, Y.; Liu, Z.; Najmaei, S.; Ajayan, P. M.; Lou, J. *Small* **2012**, *8* (7), 966−971.

(41) Lin, Y.-C.; Zhang, W.; Huang, J.-K.; Liu, K.-K.; Lee, Y.-H.; Liang, C.-T.; Chu, C.-W.; Li, L.-J. *Nanoscale* **2012**, *4* (20), 6637−6641.

(42) Shi, Y.; Huang, J.-K.; Jin, L.; Hsu, Y.-T.; Yu, S. F.; Li, L.-J.; Yang, H. Y. *Sci. Rep.* **2013**, *3*, 1839.

(43) Mertens, J.; Shi, Y.; Molina-Sánchez, A.; Wirtz, L.; Yang, H. Y.; Baumberg, J. J. *Appl. Phys. Lett.* **2014**, *104* (19), 191105.

(44) Johnson, P. B.; Christy, R. W. *Phys. Rev. B* **1972**, *6*, 4370.